Inorganic Chemistry

Article

pubs.acs.org/IC

Temperature and Magnetic Field-Assisted Switching of Magnetization and Observation of Exchange Bias in $YbCrO_3$ Nanocrystals

Preeti Gupta[§,†] and Pankaj Poddar*[,§,†,‡]

[†]Physical & Materials Chemistry Division and [‡]Center of Excellence on Surface Science, CSIR-National Chemical Laboratory, Pune 411008, India

[§]Academy of Scientific and Innovative Research, Anusandhan Bhawan, Rafi Marg, New Delhi 110001, India

Supporting Information

ABSTRACT: In this paper, we demonstrate an interesting feature in $YbCrO_3$ (YCO) nanocrystals, in which the material shows temperature and external magnetic field-assisted switching (a complete sign reversal) of zero field cooled magnetization (M_{ZFC}) and observation of exchange bias (EB) as a result of competing spin interaction at low temperature. This feature can be applied in nonvolatile memories, where, simply by changing the magnitude of the H_{ext} and T, the polarity of the magnetization can be switched between negative and positive. We also observed negative magnetization in YCO. Our results showed that, below its Nèel temperature ($T_N \approx 119$ K), the M_{ZFC} crosses over to negative sign for $H < 1000$ Oe. At 60 K, YCO showed a significant negative $M_{ZFC} \approx -0.05$ emu/g (at 100 Oe) due to the competing effects of Yb^{3+}, Cr^{3+} spins, thermal activation energy, and H_{ext}. At further lower temperatures, the M_{ZFC} showed a crossover to positive values, and the crossover temperature showed the dependence on H_{ext} (~19 K for 100 Oe curve). The YCO also showed H_{ext} and T-dependent H_{EB}, which changed its sign with T. The observed T-dependent sign reversal in the EB was closely associated with the sign reversal of M_{ZFC}. The symmetric shift in field-cooled isothermal hysteresis curves confirmed that the observed EB was not due to the unsaturated minor loop. The training cycle further confirmed that the H_{EB} value decreased to ~2% of the initial value of observed EB, which was very small compared to the observed H_{EB} in YCO, which indicated stable spin configuration at the locally formed ferromagnetic/antiferromagnetic interface.

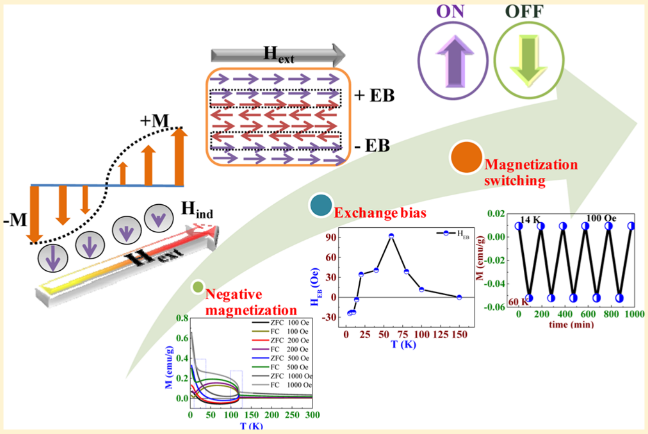

1. INTRODUCTION

Rare earth chromites ($RCrO_3$; R = rare earth element) have continued to draw the interest of researchers due to the unique features recently observed in their magnetic behavior, which are usually not observed in a large class of conventional magnetic materials.[1−11] Some of these less-understood features include external field (H_{ext}) and temperature-dependent negative magnetization (NM), EB, etc.[2,8,11] In addition, the multiferroic nature of some of these materials, where the magnetic and ferroelectric orderings coexist, has brought a lot of curiosity. On the basis of the resistivity measurements, some of the orthochromites such as $DyCrO_3$, $HoCrO_3$, $YbCrO_3$, $LuCrO_3$, and $YCrO_3$ were predicted to show ferroelectric ordering with the Curie temperature (T_c) at 803, 723, 793, 753 and 743 K, respectively.[12] The mechanism of ferroelectric ordering in these materials, which are otherwise centrosymmetric in nature, is not completely understood.[13,14] The complex nature of spin-ordering at low temperature due to competing contributions from Cr^{3+} and R^{3+} sublattices and their modifications in finite particle size also brings new science resulting from modified surface spin structure, which influences overall magnetic behavior. Recently, we reported the NM in $RCrO_3$ (R = Gd, Dy, Sm) and attributed it to T- and H_{ext}-dependent competing interaction between R^{3+} and Cr^{3+} spins.[2,8,11] In $RCrO_3$, below T_N, canted Cr^{3+} spins induce a local magnetic field on R^{3+} site, which leads to the alignment of R^{3+} spins toward the induced field (H_i). If the field H_i is stronger than H_{ext}, then NM behavior is observed.[2,8,11] Few systems, such as $GdCrO_3$,[2] $LaCr_{0.8}Mn_{0.2}O_3$,[9] $TmCrO_3$,[5] and $SmCrO_3$,[11] also show NM and tunable EB behaviors. Recently, our group also reported EB in $DyFeO_3$ orthoferrites fine particles, and we explained it by considering the core−shell model; however, the NM is more commonly reported in orthochromites in comparison to orthoferrites or any other material.[15] The reasons behind the frequent observation of NM and EB behavior in orthochro-

Received: June 27, 2015
Published: September 21, 2015

DOI: 10.1021/acs.inorgchem.5b01448
Inorg. Chem. 2015, 54, 9509−9516

mites (in contrast to orthoferrites and other such materials) are not yet understood. The EB is generally observed during field-cooled (FC) process, but recently zero-field-cooled (ZFC) EB has gained attention as it rules out the requirement of H_{ext} to shift the hysteresis loop and create unidirectional anisotropy.[6]

The anomalous behavior of $RCrO_3$ at lower temperature is very complex to understand. However, the origin of NM and EB in orthochromites can be correlated, as the sign of H_{EB} can be related to the magnetization reversal. The EB has been observed in various interfacial systems including ferromagnetic (FM)/anti-ferromagnetic (AFM), FM/ferrimagnet, FM/spin glass, core−shell structures, heterostructures, superlattices, etc.[16−21] The conventional EB is usually observed after field-cooling (FC) the material; however, in few systems, the ZFC EB is also observed.[6] The presence of multiple phases resulted in the observed ZFC EB, which was later associated with an artifact, until a model to explain the positive ZFC EB was proposed.[6] The ZFC EB was observed in $Ni_{80}Fe_{20}/Ni_{50}Mn_{50}$ alloys along with a sign reversal of EB in FC measurements.[22] Most of the previous reports either showed positive or negative EB. The H_{ext} and T-dependent sign reversal of EB is not reported so frequently. However, the polarity of EB can be changed by FC at higher applied magnetic field.[23] In few materials, the sign reversal of EB can be achieved with the change in T and magnetization reversal.[6,10]As some of the $RCrO_3$ compounds show the magnetization reversal, it will be useful to explore the possible existence of EB in this class of compounds. In addition, it is important to study the NM and EB in $RCrO_3$, as recent studies of NM and EB suggest the prospect of using these materials for applications such as spintronics and memory devices.[5,6] The materials possessing NM are useful in applications such as nonvolatile memories,[24] where, below the compensation temperature (T_{comp}—the characteristic temperature where the material exhibits a net zero magnetization) the polarity of magnetization can be flipped by changing the strength of H_{ext}.[4,10] However, instead of H_{ext}, the polarity of magnetization can also be flipped by varying the T, which is seen as an attractive option in thermomagnetic switches.[25] Similar to thermally assisted NM, the sign reversal of EB, with the change in T, is found to be useful in designing thermally assisted magnetic random access memory (MRAM).[26]

Similar to several other rare earth chromites, $YbCrO_3$ (YCO) also crystallizes in distorted orthorhombic structure with *Pbnm* space group. The strong anisotropic superexchange interaction between the Cr^{3+} and Yb^{3+} spins in YCO can induce interesting magnetic anomalies at low temperature. The YCO shows AFM ordering temperature of Cr^{3+} spins at ∼119 K and crossover temperature (T_{cross}) of ∼19.6 K with $T_{\mathrm{comp}} \approx 18.5$ K.[27] In addition, the YCO is known to be a ferroelectric at room temperature (RT) with an ordering temperature of ∼793 K, and it is known to show frequency-dependent loss tangent and dielectric constant.[28] The purpose of this study is to investigate the structural and magnetic properties of YCO. Here, we explain the behavior of NM and EB observed in YCO by detailed field- and temperature-dependent static and dynamic magnetism studies. Temperature and FC dependence of EB is also discussed in detail. The effect of temperature on the sign reversal of EB was studied, and it is correlated with the NM observed in YCO. It is the temperature, rather than field-dependent sign reversal of NM and EB in YCO, that makes it more suitable for various applications such as spintronic devices, memories, etc.

2. EXPERIMENTAL METHODS

The nanocrystalline samples of YCO were synthesized by the hydrolytic sol−gel method from ytterbium(III) nitrate hydrate ($Yb(NO_3)_3{\cdot}xH_2O$, Aldrich, 99.9% metal basis), chromium nitrate ($Cr(NO_3)_3$, Thomas baker, 99.9%) and citric acid without any further purification.[8,11] Powder X-ray diffraction (PXRD) data were collected at RT on a PANalytical X'PERT PRO instrument using Cu Kα radiation (2θ range of 20−80°, a step width of 0.02°, and $\lambda = 1.54$ Å). The morphology of YCO particles was obtained by using FEI Tecnai F30 high-resolution transmission electron microscope (HRTEM) operated at 300 kV. X-ray photoelectron spectroscopy (XPS) data were collected using VG Microtech, model ESCA 3000, equipped with ion-gun (EX-05) for cleaning the surface. The binding energy resolution was 0.1 eV; however, the overall resolution was limited to the bandwidth of X-ray source (∼1 eV). Here, we used the Shirley algorithm for the background correction. Raman spectra were recorded using He−Ne laser of wavelength 632 nm coupled with a Labram-HR800 micro-Raman spectrometer using a 100 X objective. The magnetic measurements were performed using a Physical Property Measurement System (PPMS; Quantum Design Inc., San Diego, California) equipped with a 9 T superconducting magnet. We performed direct-current (DC) magnetization versus temperature (M−T) and magnetization versus magnetic field (M−H) measurements using a vibrating sample magnetometer (VSM) attachment and alternating-current (AC) magnetizations versus temperature using ACMS attachment. The degauss procedure was followed carefully to nullify the trapped field in the superconducting magnet.

3. RESULTS AND DISCUSSION

3.1. X-ray Diffraction. The Figure 1 shows the PXRD diffraction pattern of YCO nanocrystallites. The peaks were indexed with an orthorhombic perovskite structure having *Pbnm* space group according to JCPDS file No. 25−1076. The lattice parameters of YCO particles were found to be $a = 5.18$, $b = 5.48$, and $c = 7.5$ Å, which agreed well with the previously reported values.[27] These results clearly demonstrated the formation of pure phase of YCO, with no observed impurity peak. The average crystallite size of YCO nanocrystallites was calculated using Debye−Scherer method and was found to be ∼70 nm.

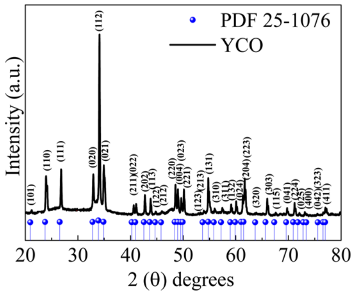

Figure 1. Powder XRD pattern of YCO nanocrystallites with reference data (shown in blue).

3.2. Morphological Studies. The Figure 2a shows the representative transmission electron microscopy (TEM) image of YCO nanocrystallites, indicating platelike structure. The inset shows the expanded scale view of the dotted region as shown in Figure 2a. The average particle size of YCO was found to be ∼80 nm. The HRTEM image in the Figure 2b shows the good crystallinity with interplanar spacing $d \approx 0.33$ nm corresponding to (112) plane of YCO lattice, which is also the most intense peak in the XRD pattern. In TEM images, we also observed that often two or more nanoplatelets are fused

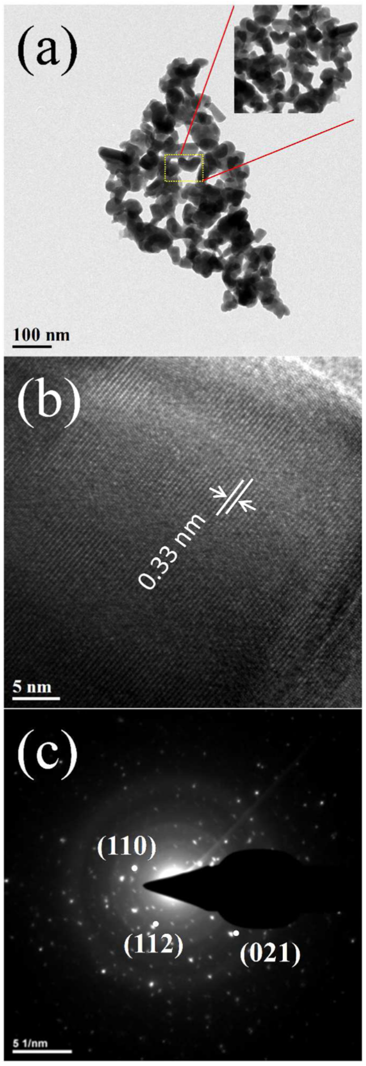

Figure 2. (a) The bright-field TEM image show platelike morphology with average particle size of ∼80 nm. (inset) Expanded view of the dotted. (b) The HRTEM image shows lattice fringes corresponding to (112) plane of the YCO crystal. (c) The SAED pattern of YCO polycrystallites.

together. In addition, the formation of platelike structure can be understood by considering the role of nitrate and citrate ions.[2,8] It is well-known that the faceted growth of crystal is affected and altered by the intrinsic crystal structure and other parameters such as reaction conditions, that is, the kinetic energy barrier, temperature, time, and capping molecules.[29,30] In general, ligands or surfactants preferentially bind the facets having higher surface energy restricting the growth along this facet though other factors also play some role as the overall charge at the surface (cation/anion ratio), relative binding affinity of various functional groups of the molecules to various surfaces.[31]Apart from the role of nitrate and citrate in governing the morphology of the particles, there are various other factors such as twinning, stacking faults.[8] The citric acid used here acts as a chelating agent, and it also governs the morphology of the particle. From our previous studies, we observed that the chelating agent, that is, citric acid and oxalic acid, plays an important role in the phase formation of $DyCrO_3$ nanoparticle; we found that the formation of a chelate ring is much stronger in the citric acid-assisted synthesis, and it forms more stable complexes than oxalates.[8] Also, the number of ionizable groups present in the citric and oxalic acid usually influences the combustion process, and the energy released from the exothermic reaction is different, thereby affecting the phase formation.[8] Thus, the tridentate nature of citric acid forms more stable metal complex. The molar ratio of citrate to nitrate also plays a significant role in determining the platelike morphology of YCO. The citrate ion has a function to inhibit the longitudinal growth of crystals along the ⟨001⟩ with the enhancement in the sideways growth giving two-dimensional platelike structure, similar to what is observed when sodium citrate, citric acid, or phosphate ions are used.[32−35] Similarly, as YCO crystallizes in orthorhombic structure, the citrate ions preferentially bind on ⟨001⟩ facets having higher density of atoms and thus restrict its growth longitudinally, which results in the platelike morphology as shown in Scheme 1. However, the increase in the citrate and nitrate molar ratio will, in turn, lead to the suppression of the growth sideways by the adsorption of more citrate ions resulting in the reduction of thickness of the crystals. Thus, molar ratio 1:1 and role of citric acid found to be favorable for the YCO nanoplatlets formation.[31] The Figure 2c represents the selected area electron diffraction (SAED) pattern with diffraction spots and rings corresponding to planes (021), (112), and (110) for YCO, respectively, indicating the crystalline nature of YCO. In addition, to further reveal the chemical composition and oxidation states and Raman modes associated with YCO, X-ray photoelectron spectroscopy (XPS) and Raman spectroscopy measurements were done and shown in Figures S1a−c and Figure S2 [see Supporting Information].

Scheme 1. Schematic Showing the Formation of Platelike Morphology of Orthorhombic Perovskite YCO Nanocrystals

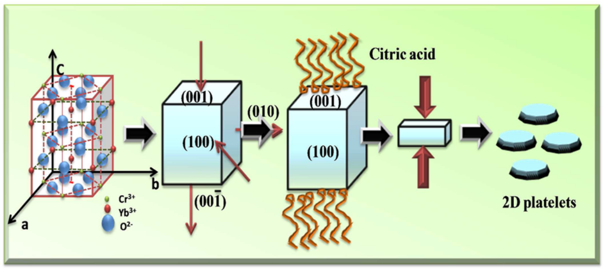

3.3. Magnetic Studies. The Figure 3a shows the ZFC and FC magnetization (M_{ZFC}, M_{FC}) versus T curves of YCO at H_{ext} = 100 Oe in a temperature (T) range from 3 to 300 K. At RT, the YCO shows paramagnetic behavior and Cr^{3+} spins order antiferromagnetically below $T_N \approx 119$ K, which is close to the Néel transition temperature reported for YCO single crystal.[36] It was observed that, just below the T_N, the M_{ZFC} shows a positive value with a shoulder, before decreasing at further lower temperatures as shown in the lower right panel of Figure 3a. This is the characteristic feature of AFM transitions. With further decrease in T, M_{ZFC} crossed $M_{ZFC} = 0$ line at $T_{comp(1)} \approx$ 117 K (compensation temperature) and turned negative in its sign. The NM observed in YCO can be attributed to the increase in the induced field (H_i) on Yb^{3+} spins due to the canted Cr^{3+} spins with respect to H_{ext} = 100 Oe. The M_{ZFC} decreases further to reach a minimum value of ca. −0.055 emu/g at 60 K. The M_{ZFC} turns again positive below $T_{comp(2)} \approx 19$ K. However, below T_N, the M_{FC} value increases because Yb^{3+} and Cr^{3+} spins were coupled together contributing to the net M_{FC}

DOI: 10.1021/acs.inorgchem.5b01448
Inorg. Chem. 2015, 54, 9509−9516

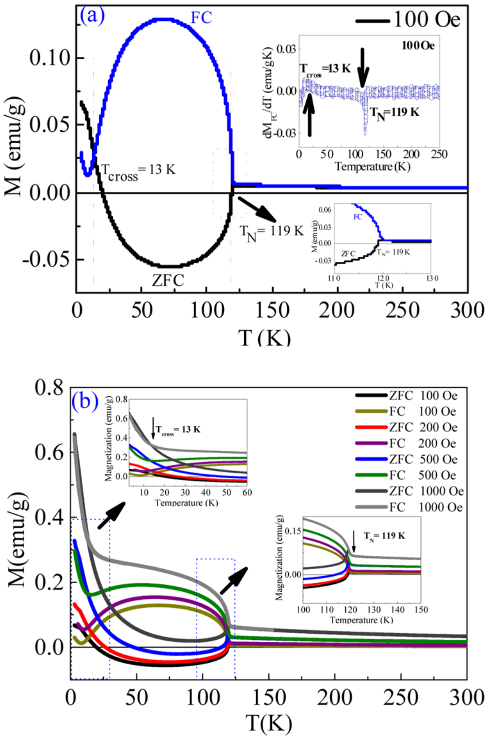

Figure 3. (a) The $M_{ZFC}(T)$−$M_{FC}(T)$ curves at $H_{ext} \approx 100$ Oe with an inset at upper right showing dM_{FC}/dT plot of YCO polycrystallites and lower right shows the expanded view at T_N. (b) Field-dependent $M_{ZFC}(T)$−$M_{FC}(T)$ curves where $M_{ZFC}(T)$ curves clearly indicating a crossover from negative to positive magnetization at larger H_{ext}. (insets) Expanded view of $M_{ZFC}(T)$−$M_{FC}(T)$ curves near (upper left) T_{cross} and (lower right) T_N, respectively, as indicated by dotted boxes.

value, reaching a maximum of ca. +0.129 emu/g at ~60 K (in the proximity to the point where M_{ZFC} shows a minimum). Below 60 K, M_{FC} decreases, reaching a minimum value of ~0.012 emu/g at ~9 K. We also observed $T_{cross} \approx 13$ K (crossover temperature at which M_{ZFC} and M_{FC} crosses), which further passes through zero at the compensation temperature $T_{comp(2)} \approx 19$ K. As seen from the Figure 3a, the observed $T_{comp(2)} \approx 19$ K was slightly higher than the reported values for bulk YCO $T_{comp(2)} \approx 18.3$ and ~16.5 K,[27,36] which can be due to the particle size of the compound. The upper right panel in Figure 3a shows the temperature-dependent derivative of M_{FC}. From the dM_{FC}/dT versus T curve, we observe prominent peaks situated at ~119 and ~13 K, respectively. These peaks are consistent with the magnetic transitions observed in M_{FC} versus T.

Detailed external magnetic field-dependent $M_{FC}(T)$ and $M_{ZFC}(T)$ studies were done to understand the NM behavior in YCO. The Figure 3b shows the field-dependent M_{ZFC}−T and M_{FC}−T curves. The expanded views around T_{cross} (upper left) and T_N (lower right) are depicted in Figure 3b. The $T_{comp(1)}$ was found to be field-dependent, which monotonically decreases from ~117 to ~113 K as we increased the H_{ext} from 100 to 500 Oe. At $H_{ext} \leq 500$ Oe, the NM observed was because the canting of Cr^{3+} spins induces local magnetic field on Yb^{3+}spins, which results in an antiparallel alignment of Cr^{3+} and Yb^{3+} spins. At 1000 Oe, the H_{ext} overcame the induced magnetic field giving positive magnetization in YCO. The quantitative measure of NM in YCO was given by the ratio of negative to positive magnetization $M_{-ive}/M_{+ive} = M_{ZFC}/M_{FC}$, that is, the minimum and maximum values of $M_{ZFC}(T)$ and $M_{FC}(T)$ curves, which was found to be −0.4 for $H_{ext} = 100$ Oe. In some of the polycrystalline rare earth chromites such as $GdCrO_3$, $La_{0.5}Pr_{0.5}CrO_3$, and $LaCr_{0.85}Mn_{0.15}O_3$, these values are reported to be 30, 40, and 2 for 100 Oe applied magnetic field.[37−39] However, after increasing the H_{ext}, this ratio decreases to −0.25 at 200 Oe and to −0.09 at 500 Oe. Similarly, the relative irreversible magnetization calculated using $\Delta M/M_{ZFC} = (M_{FC} - M_{ZFC})/M_{ZFC}$, for YCO was found to be −1.4, which is comparable to $GdCrO_3$, $La_{0.5}Pr_{0.5}CrO_3$, and $LaCr_{0.85}Mn_{0.15}O_3$ polycrystallites having values in the range from −2 to −9.[37−39]

As EB is known to be associated with the NM; therefore, the observation of NM below $T_N \approx 119$ K prompted us to explore the possibility of EB behavior in YCO nanocrystallites. The M−H loops were measured in a broad temperature range (5−100 K) in ZFC condition and shown in Figure 4. As seen from the Figure 4a, the linear behavior at RT indicates the paramagnetic nature of YCO. Below T_N, we observed an opening of M−H loop and lack of saturation, attributed to the canted AFM ordering of Cr^{3+} spins.[2,8,11] However, we noticed an asymmetry in hysteresis loops, as the sample was cooled from 100 to 20 K (Figure 4b−f). The H_{EB} was found to switch from positive to negative at ~13 K. The sign-reversal temperature of H_{EB} from positive to negative, while cooling, was also found to be consistent with the sign reversal of M_{ZFC} (disappearance of NM). Below 10 K, as shown in Figure 4g,h, the system shows negative exchange bias (NEB). In general, the competition between weak FM and strong AFM results in the shift of hysteresis toward the negative side of origin.

3.3.1. Study of Temperature-Dependent Exchange Bias and Its Origin.

As seen from the Figure 5a, the H_{EB} at 100 K was found to be ~12 Oe, which reached to maximum of ~93 Oe at 60 K. This initial increase in H_{EB} was mainly due to the increase in the ordering of Yb^{3+} AFM spins toward the canted Cr^{3+} FM spins giving weak FM component with the decrease in T. After cooling below 60 K, we observed $H_{EB} \approx 41$ Oe at 40 K and ~34 Oe at 20 K. This decrease in H_{EB} can be related with the change in the slope of M_{ZFC} below 60 K where, after reaching NM_{max}, the M_{ZFC} values start increasing and cross $M_{ZFC} = 0$ at ~13 K. After the temperature is reduced further, H_{EB} turned negative and decreased from ca. −4 Oe at 14 K (T_{cross}) to ca. −24 Oe at 5 K due to the increasing Yb^{3+}−Yb^{3+} AFM superexchange interaction, which normally appears at very low temperature.

The temperature-dependent EB reversal can be explained by considering the NM behavior in YCO. The anisotropic exchange interaction between canted Cr^{3+} spins and Yb^{3+} spins under the influence of H_i leads to EB in YCO. Below T_N (~119 K), the H_{EB} increases until 60 K, which is mainly owing to the increase in the magnitude of AFM component of paramagnetic Yb^{3+} spins due to the canted Cr^{3+} spins until the induced field is negative. Therefore, a large positive field was required to bring the magnetization back to the positive value and cross zero value giving positive exchange bias (PEB). As soon as the magnetization became positive and reached the compensation temperature ($T_{comp(2)} \approx 19$ K), the magnitude of H_{EB} became negative. The sign reversal of H_{EB} can be explained by the relation $H_{EB} \approx -M$.[5,40,41] At low T, the long-range AFM ordering of Yb^{3+}−Yb^{3+}spins dominates and results in the decrease of Yb^{3+}−Cr^{3+} magnetic interaction. Moreover, because of the NM, a downward shift in M−H curve results in PEB and vice versa.[4,5] The Figure 5b showed the decrease in H_C from ~1610 to ~2 Oe with the decrease in T from 100 to 7 K. The

DOI: 10.1021/acs.inorgchem.5b01448
Inorg. Chem. 2015, 54, 9509−9516

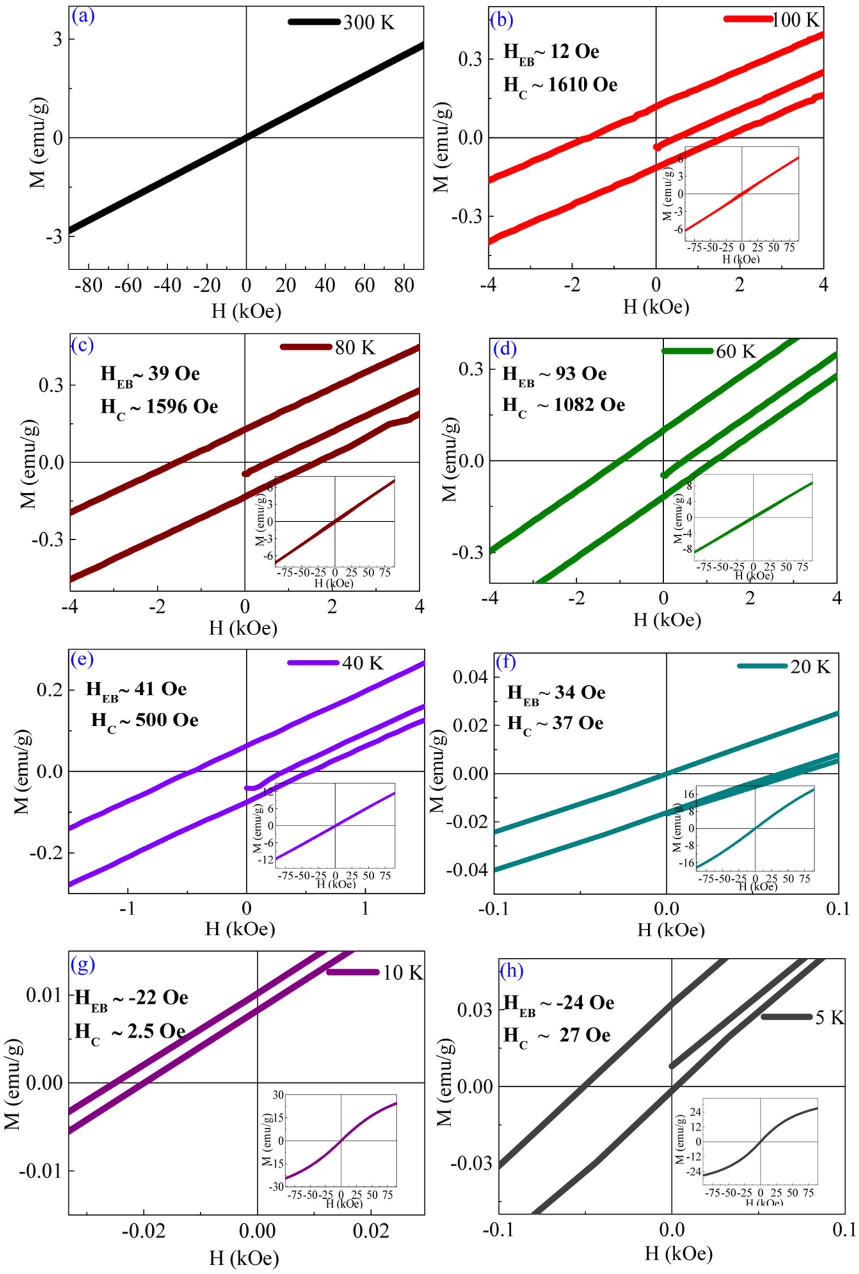

Figure 4. Expanded view of $M-H$ curves of YCO nanocrystallites at varying temperatures showing switching of exchange bias (H_{EB}) from positive to negative as indicated in the panels. Each panel shows the H_{EB} and H_C values of YCO at different temperatures. (insets) The full $M-H$ loops in −90 to +90 kOe field-sweep.

weak FM ordering gives rise to a noticeable coercivity in the temperature range of 100−20 K suggesting the presence of large FM component of canted Cr^{3+} spins. The decrease in H_C can be attributed to the strong AFM interaction of $Yb^{3+}-Yb^{3+}$ spins at low T.

3.3.2. Effect of Field Cooling on Exchange Bias in YCO.

The conventional exchange bias (CEB) at 60 K was measured by cooling under various external fields H_{FC} (−2, −5, and −10 kOe). The results are compared in Figure 6a with an inset (upper left) showing the zoomed view. The $M-H$ loops were found to be elliptical indicating the predominant AFM interaction with weak FM arising due to the canted Cr^{3+} spins. As shown in lower right of Figure. 6a, the H_{EB} was found to be ca. −377 Oe at −2 kOe, and with the increase in H_{FC} from −5 to −10 kOe, the $H_{EB} \approx -375$ Oe decreased to ca. −360 Oe. This NEB effect became further weaker with the increase in H_{FC} (−10 kOe). The effect of change in polarity of applied magnetic field while field cooling (H_{FC}) on the $M-H$ loop parameter of YCO was measured at H_{FC} ± 10 kOe (Figure 6b). The H_{EB} and H_C values were found to be ∼759 and ∼1082 Oe, respectively; the H_{EB} values remain the same, but their sign reverses with the sign reversal in $\pm H_{FC}$ as shown in the Table (inset of Figure 6b). The applied H_{FC} was comparatively more than the observed H_C of YCO at 60 K. Thus, at this field H_{FC}, Yb^{3+} and Cr^{3+} spins follow the direction of H_{FC} and orient itself in such a fashion so as to give FM coupling resulting in NEB. However, by changing the polarity of H_{FC}, the H_{EB} changes accordingly. The $M-H$ loops shifted toward the left side of the origin at −10 kOe but symmetrically opposite to what were observed for +10 kOe. This symmetric

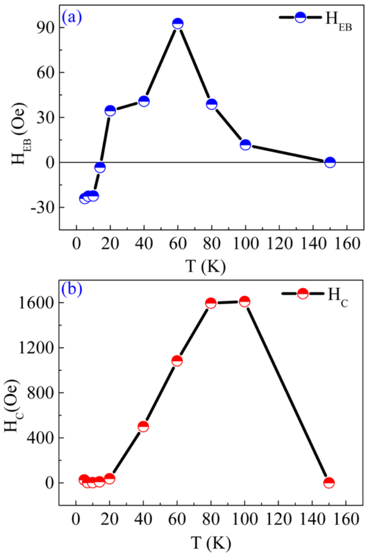

Figure 5. Temperature variation of (a) exchange bias H_{EB} and (b) coercive field H_C of YCO nanocrystallites in ZFC condition. Switching of H_{EB} from positive to negative can be seen with the decrease in temperature, which is consistent with the magnetic transitions seen in the $M_{ZFC}(T)$−$M_{FC}(T)$ curves.

shift also confirmed that the EB observed is not due to the unsaturated minor loop but due to the uncompensated spins at the FM/AFM interface.[6,16,42]

3.3.3. Training Effect on Exchange Bias. As we noticed in the M_{ZFC}, M_{FC} versus T curves (Figure 3b), for $H_{ext} \approx 1$ kOe, the M_{ZFC} remains positive at all the measured T range (i.e., it does not show NM). At $H_{FC} = 10$ kOe, the canted AFM spins align in the field direction and drag the Yb^{3+} spins along the Cr^{3+} spins, thereby making the interfacial interaction FM. Thus, the NEB was observed, which goes well with the relation $H_{EB} \approx -M$. In conventional systems, the training effect is considered to be one of the best methods to study the EB. Repeating the hysteresis loop a number of times leads to the relaxation of uncompensated spins at the interface making M−H loop increasingly symmetric.[5,16,43] The training effect in H_{EB} was measured after applying H_{FC} + 10 kOe as shown in Figure 6c. With the increasing number of cycles (n), H_{EB} value decreased to 2% from $n = 0$ to $n = 4$ at 60 K, which is very small when compared to the observed EB in YCO nanocrystallites. This indicates that the spin configuration was quite stable at the interface even against the applied magnetic field, and after each cycle, the AFM spin tries to find an energetically favorable condition.[4,6,16] Similarly, H_C also follows the H_{EB} (Figure 6d) and decreases with the increase in the loop cycle.

3.3.4. Temperature and Field-Assisted Memory-Switching Application. The sign reversal of EB and magnetization, as shown by us, holds promise toward its application in thermal-assisted memory switching.[44,45] As we discussed earlier, the temperature dependence of NM was in agreement with the observed temperature dependence on EB. To demonstrate the switching effect for possible applications, magnetization switching was performed by varying T and H_{ext}. Figure 7a showed the switching of M_{ZFC} between negative to positive by switching T from 60 to 14 K at 100 Oe applied external magnetic field. Similarly, the NM observed in ZFC magnetization curve at 100 Oe can be flipped to positive by applying H_{ext} = 1000 Oe, as shown in Figure 7b. In YCO nanocrystallites, the characteristic feature of magnetization flipping from negative to positive, by simply changing the T, is different from conventional magnetic materials, where H_{ext} is required to change the polarity. The polarity switching of the magnetization by varying T and H_{ext} was further probed by cycling several times; these features showed good reproducibility, and no noticeable decay was observed. Thus, the magnetization can be tuned in a predictable way, and this behavior is favorable for subtle application in

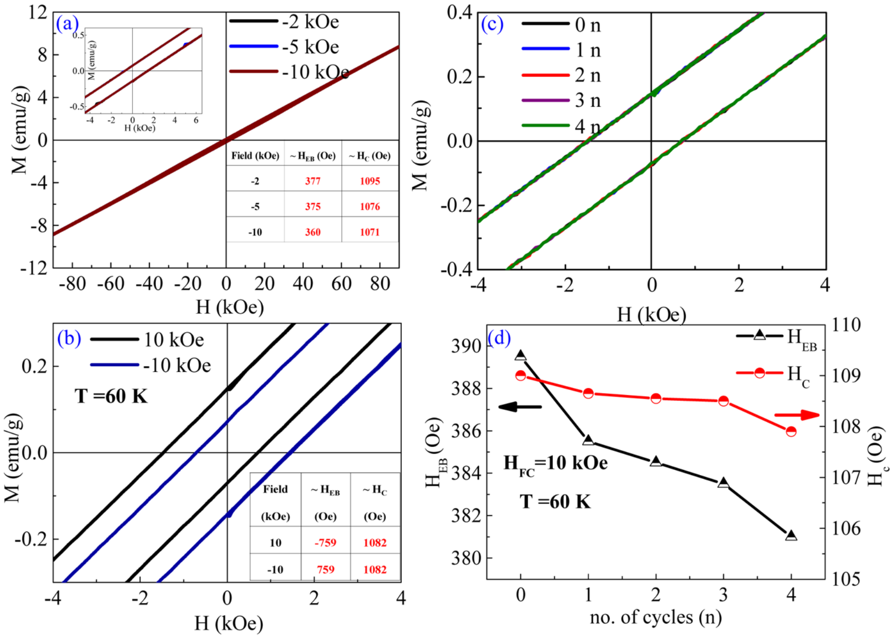

Field (kOe)	~ H_{EB} (Oe)	~ H_C (Oe)
-2	377	1095
-5	375	1076
-10	360	1071

Field (kOe)	~ H_{EB} (Oe)	~ H_C (Oe)
10	-759	1082
-10	759	1082

Figure 6. (a) Effect of field-cooling on the EB of YCO nanocrystallites at different H_{ext}. (upper left inset) Expanded view of shift of hysteresis curve with field cooling and (lower right) showing the change in coercivity (H_C) and exchange bias field (H_{EB}) with the change in H_{FC} (b) representing the effect of applied magnetic field ±10 kOe on M−H curve of YCO. (c) Effect of training cycle on H_{EB}. (d) Decrease in H_{EB} and H_C with an increase in number of measurement cycle (n).

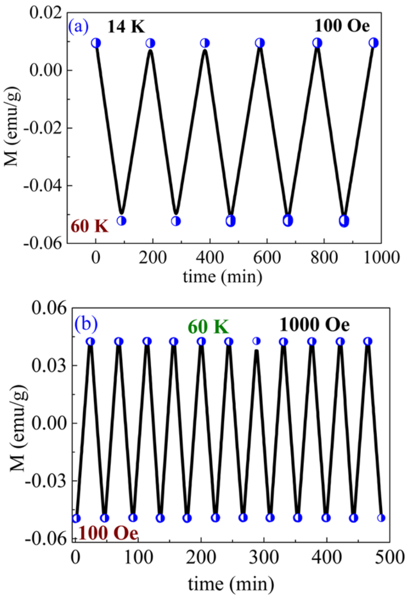

Figure 7. (a) The figure shows magnetization switching from negative to positive values with the switching in T from 60 to 14 K in ZFC condition at 100 Oe external magnetic field. (b) The figure shows switching of magnetization while changing H_{ext} from 100 to 1000 Oe at 60 K.

nonvolatile magnetic memories.[44] Similar feature was also observed in other chromites exhibiting NM such as $YFe_{0.5}Cr_{0.5}O_3$,[44] $SmCr_{1-x}Fe_xO_3$,[45] and $TmCrO_3$.[5]

3.4. Temperature and Frequency-Dependent Alternating Current Magnetization Studies. The AC-magnetization measurement is an extremely sensitive technique to detect magnetic anomalies such as Nèel transition, reversible rotation of magnetic moments, spin glass transition, or small impurities in a single-phase multiferroic.[46] The AC-magnetic measurements were done at a 10 Oe excitation field without any applied DC bias in a range of frequencies (between 501 and 9999 Hz). Figure 8a,b represents the real part of AC-magnetization (M') curves in temperature ranges of 10−25 and 115−125 K, respectively. At low temperature (Figure 8a), we did not detect any anomaly. However, the measurements in the vicinity of T_N showed a weak anomaly at $T_N \approx 119$ K in the $M'-T$ curve, which agrees well with the DC-magnetic measurements (inset shows the expanded view at T_N). We cannot ignore the fact that surface effects play an important role in determining the magnetic properties of the nanoscale materials. AC-magnetic measurements are a highly sensitive and efficient tool to detect any spin-glass-type of behavior often associated with the super-paramagnetic state of the nanoparticles in the frequency dependence magnetic susceptibility in a system. We did not find any frequency dependence of M' in YCO or any such behavior in the DC magnetization that could be linked to the blocking transition in YCO.

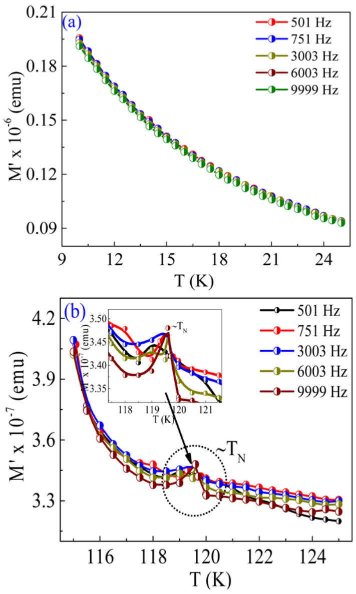

Figure 8. Temperature and frequency dependence of the real part of the AC magnetization curves measured at a 10 Oe AC field (a) 10−25 K and (b) 115−125 K for YCO. (b, inset) The expanded views of the real component of the AC magnetization curves around $T_N \approx 119$ K.

■ CONCLUSIONS

In the present work, YCO was successfully synthesized using hydrolytic sol−gel method. The XRD pattern clearly demonstrates the formation of orthorhombic single-phase YCO nanocrystallites. The TEM images show the formation of platelet-like structure with an average particle size ~80 nm. The YCO shows NM below T_N; with the decrease in T, its sign reverses, and the magnetization becomes positive just below $T_{comp(2)}$. The switching of PEB to NEB can be related to the sign reversal of magnetization with the decrease in T. The effect of field cooling and training cycle demonstrated that the EB observed was not due to unsaturated minor loop and thus confirmed the EB behavior of YCO. The existence of simultaneous negative and positive magnetization offers thermal-assisted switching of magnetization in YCO. The YCO also possesses the switching characteristic merely by changing the magnitude rather than the direction of applied magnetic field. Thus, coexistence of sign reversal of NM and EB makes YCO a potential candidate for spintronics and memory based devices.

■ ASSOCIATED CONTENT

Ⓢ Supporting Information

The Supporting Information is available free of charge on the ACS Publications website at DOI: 10.1021/acs.inorgchem.5b01448.

> Discussion of the X-ray photoelectron spectroscopy and Raman spectroscopy studies of $YbCrO_3$ nanocrystals. Core level XPS spectra of (a) Cr (2p), (b) O (1s), and (c) Yb (4d) in YCO, room-temperature Raman spectra of YCO nanocrystallites, Raman peak positions corresponding to various modes (tabulated). (PDF)

■ AUTHOR INFORMATION

Corresponding Author

*E-mail: p.poddar@ncl.res.in. Phone: +91-20-2590-2580. Fax: +91-20-2590-2636.

Notes

The authors declare no competing financial interest.

■ ACKNOWLEDGMENTS

P.P. acknowledges support from Young Scientist Award grant from Council for Scientific and Industrial Research (CSIR) in Physical Sciences and a separate grant from Dept of Science &

Technology, India (DST/INT/ISR/P-8/2011). P.G. acknowledges the support from the CSIR, India, for providing Senior Research Fellowship.

■ REFERENCES

(1) Cooke, a H.; Martin, D. M.; Wells, M. R. *J. Phys. C: Solid State Phys.* **1974**, *7*, 3133−3144.
(2) Jaiswal, A.; Das, R.; Vivekanand, K.; Maity, T.; Abraham, P. M.; Adyanthaya, S.; Poddar, P. *J. Appl. Phys.* **2010**, *107* (1), 013912.
(3) Sardar, K.; Lees, M. R.; Kashtiban, R. J.; Sloan, J.; Walton, R. I. *Chem. Mater.* **2011**, *23* (1), 48−56.
(4) Yoshii, K. *Appl. Phys. Lett.* **2011**, *99* (14), 142501.
(5) Yoshii, K. *Mater. Res. Bull.* **2012**, *47* (11), 3243−3248.
(6) Krishna Murthy, J.; Venimadhav, a. *Appl. Phys. Lett.* **2013**, *103* (25), 0−5.
(7) Srinu Bhadram, V.; Rajeswaran, B.; Sundaresan, a.; Narayana, C. *EPL (Europhysics Lett.* **2013**, *101* (1), 17008.
(8) Gupta, P.; Bhargava, R.; Das, R.; Poddar, P. *RSC Adv.* **2013**, *3* (48), 26427.
(9) Bora, T.; Ravi, S. *J. Magn. Magn. Mater.* **2014**, *358−359*, 208−211.
(10) Cao, Y.; Cao, S.; Ren, W.; Feng, Z.; Yuan, S.; Kang, B.; Lu, B.; Zhang, J. *Appl. Phys. Lett.* **2014**, *104* (23), 1−5.
(11) Gupta, P.; Bhargava, R.; Poddar, P. *J. Phys. D: Appl. Phys.* **2015**, *48* (2), 025004.
(12) Rao, G. V. S.; Wanklyn, B. M.; Rao, C. N. R. *J. Phys. Chem. Solids* **1971**, *32*, 345−358.
(13) Ramesha, K.; Llobet, a; Proffen, T.; Serrao, C. R.; Rao, C. N. R. *J. Phys.: Condens. Matter* **2007**, *19* (10), 102202.
(14) Rajeswaran, B.; Khomskii, D. I.; Zvezdin, a. K.; Rao, C. N. R.; Sundaresan, a. *Phys. Rev. B: Condens. Matter Mater. Phys.* **2012**, *86* (21), 1−5.
(15) Jaiswal, A.; Das, R.; Maity, T.; Poddar, P. *J. Appl. Phys.* **2011**, *110* (12), 124301.
(16) Nogués, J.; Schuller, I. K. *J. Magn. Magn. Mater.* **1999**, *192* (2), 203−232.
(17) Berger, a.; Hovorka, O.; Friedman, G.; Fullerton, E. E. *Phys. Rev. B: Condens. Matter Mater. Phys.* **2008**, *78* (22), 1−6.
(18) Berger, a.; Margulies, D. T.; Do, H. *J. Appl. Phys.* **2004**, *95* (11), 6660−6662.
(19) Won, C.; Wu, Y. Z.; Arenholz, E.; Choi, J.; Wu, J.; Qiu, Z. Q. *Phys. Rev. Lett.* **2007**, *99* (7), 1−4.
(20) Schulz, B.; Baberschke, K. *Phys. Rev. B: Condens. Matter Mater. Phys.* **1994**, *50* (18), 13467−13471.
(21) Hong, T. M. *Phys. Rev. B* **1998**, *58* (1), 10.
(22) Saha, J.; Victora, R. H. *Phys. Rev. B: Condens. Matter Mater. Phys.* **2007**, *76* (10), 1−4.
(23) Hong, F.; Cheng, Z.; Wang, J.; Wang, X.; Dou, S. *Appl. Phys. Lett.* **2012**, *101*, 102411.
(24) Mandal, P.; Sundaresan, a.; Rao, C.; Iyo, a.; Shirage, P.; Tanaka, Y.; Simon, C.; Pralong, V.; Lebedev, O.; Caignaert, V.; Raveau, B. *Phys. Rev. B: Condens. Matter Mater. Phys.* **2010**, *82* (10), 1−4.
(25) Yusuf, S. M.; Kumar, A.; Yakhmi, J. V. *Appl. Phys. Lett.* **2009**, *95* (18), 11−14.
(26) Prejbeanu, I. L.; Kerekes, M.; Sousa, R. C.; Sibuet, H.; Redon, O.; Dieny, B.; Nozières, J. P. *J. Phys.: Condens. Matter* **2007**, *19* (16), 165218.
(27) Su, Y.; Zhang, J.; Feng, Z.; Li, L.; Li, B.; Zhou, Y.; Chen, Z.; Cao, S. *J. Appl. Phys.* **2010**, *108* (1), 013905.
(28) Rao, C. N. R.; Serrao, C. R. *J. Mater. Chem.* **2007**, *17* (47), 4931.
(29) Lee, S. M.; Cho, S. N.; Cheon, J. *Adv. Mater.* **2003**, *15* (5), 441−444.
(30) Lu, H. B.; Liao, L.; Li, H.; Wang, D. F.; Li, J. C.; Fu, Q.; Zhu, B. P.; Wu, Y. *Phys. E* **2008**, *40* (9), 2931−2936.
(31) Lu, H.; Wang, S.; Zhao, L.; Dong, B.; Xu, Z.; Li, J. *RSC Adv.* **2012**, *2* (8), 3374.
(32) Padhye, P.; Poddar, P. *J. Mater. Chem. A* **2014**, *2* (45), 19189−19200.
(33) Tian, Z. R.; Voigt, J. a.; Liu, J.; Mckenzie, B.; Mcdermott, M. J. *J. Am. Chem. Soc.* **2002**, *124* (44), 12954−12955.
(34) Liang, J.; Liu, J.; Xie, Q.; Bai, S.; Yu, W.; Qian, Y. *J. Phys. Chem. B* **2005**, *109* (19), 9463−9467.
(35) Imai, H.; Iwai, S.; Yamabi, S. *Chem. Lett.* **2004**, *33* (6), 768−769.
(36) Shtrikman, S.; Wanklyn, B. M.; Y, I. *Int. J. Magn.* **1971**, *1*, 327.
(37) Yoshii, K. *J. Solid State Chem.* **2001**, *159* (1), 204−208.
(38) Sharma, N.; Srivastava, B. K.; Krishnamurthy, A.; Nigam, a. K. *Solid State Sci.* **2010**, *12* (8), 1464−1468.
(39) Bora, T.; Ravi, S. *J. Appl. Phys.* **2013**, *114* (18), 0−5.
(40) Manna, P. K.; Yusuf, S. M.; Shukla, R.; Tyagi, a. K. *Appl. Phys. Lett.* **2010**, *96* (24), 2−4.
(41) Singh, R. P.; Tomy, C. V.; Grover, A. K. *Appl. Phys. Lett.* **2010**, *97*, 182505.
(42) Manna, P. K.; Yusuf, S. M. *Phys. Rep.* **2014**, *535* (2), 61−99.
(43) Binek, C. *Phys. Rev. B: Condens. Matter Mater. Phys.* **2004**, *70* (1), 1−5.
(44) Mao, J.; Sui, Y.; Zhang, X.; Su, Y.; Wang, X.; Liu, Z.; Wang, Y.; Zhu, R.; Wang, Y.; Liu, W.; Tang, J. *Appl. Phys. Lett.* **2011**, *98* (19), 3−6.
(45) Yin, L. H.; Liu, Y.; Tan, S. G.; Zhao, B. C.; Dai, J. M.; Song, W. H.; Sun, Y. P. *Mater. Res. Bull.* **2013**, *48* (10), 4016−4021.
(46) Pütter, S.; Ding, H.; Millev, Y.; Oepen, H.; Kirschner, J. *Phys. Rev. B: Condens. Matter Mater. Phys.* **2001**, *64* (9), 10−13.